Journal of Nanoscience and Nanotechnology
Vol. 10, 1508–1524, 2010

REVIEW

Microresonators in CMOS Compatible Substrate*

Siva Yegnanarayanan, Mohammad Soltani, Qing Li, Ehsan Shah Hosseini, Ali A. Eftekhar, and Ali Adibi*

School of Electrical and Computer Engineering, Georgia Institute of Technology, 777 Atlantic Dr NW, Atlanta, Georgia 30332, USA

We report our recent progress in designing and developing traveling-wave microresonators on CMOS compatible substrate, with a focus on ultra-compact Si-based microring and microdisk resonators in the visible and near infrared wavelengths with ultra-high Q and small mode volume, suitable for strong light-matter interaction. The performance of these resonators is discussed, and the design and fabrication challenges and solutions to achieve efficient coupling from the bus-waveguide to the resonator is mentioned. Coupled-resonator architectures for the design of filters are analyzed and theoretical and experimental results for the flat-band filters with wide bandwidth and large free spectral range are presented. Furthermore, by using a detailed thermal model we demonstrate optimized microresonator structures on semiconductor substrates with improved thermal conductivity that can sustain a high circulating optical intensity at the resonance wavelength, which is particularly useful for nonlinear optics and optical signal processing applications. Finally, we address some of the applications and future prospects of such microresonators in CMOS-compatible substrate technology, including portable multi-purpose bio/chemical sensing systems, reconfigurable optical signal processing modules and chip-scale optical amplifiers and lasers.

Keywords: Microresonators, Photonics, Sensing.

CONTENTS

1. INTRODUCTION

Microresonators, characterized by the circulation of light within dielectric volumes, enables storage of optical power near specific resonant frequencies and is important in a wide range of fields including cavity quantum electrodynamics,[1] photonics,[2] biosensing[3,4] and nonlinear optics.[5] While the first microring resonators were proposed as integrated optical wavelength filters by Marcatili in 1969,[6] emerging applications such as photonic interconnects,[7,8] optical signal processing,[9,10] optofluidics[11] and chip-scale biosensors,[12,13] which require high-levels of optical functionalities in chip-scale devices, is driving the need for an integrated platform with wavelength-scale resonator sizes. However, there are two major challenges in realizing such chip-scale, ultra-high Q microresonators. The first is finding a high-index contrast material system in which low-loss optical waveguides can be fabricated and the second is the ability to lithographically pattern very narrow gaps that are essential for coupling the microresonators to each other and to the input and output bus waveguides. With the rapid evolution in the fabrication technology in the early 1990's, it has become feasible to realize sub-100 μm microresonator structures with good optical performance, in several different material systems such as III–V semiconductor substrates e.g., InP, GaAs as well as III–N such as GaN, dielectrics such as silica, polymers as well as ferroelectrics such as Lithium Niobate.[14,15]

In this paper we focus primarily on traveling-wave microresonators in Si-CMOS compatible substrate technology and report on the latest developments as well as the tremendous amount of progress that has been achieved recently in their design and fabrication, which

*Author to whom correspondence should be addressed.
*This is an invited review paper.

1533-4880/2010/10/1508/017 doi:10.1166/jnn.2010.2029

Siva Yegnanarayanan received his B.Tech. in Electrical Engineering in 1993 from Indian Institute of Technology (IIT) Madras. Following his Ph.D. in 1999 from the University of California, Los Angeles (UCLA) in Electrical Engineering, with a specialization in Photonics, he worked as a Research Scientist at Alcatel Corporate Research Center, Dallas on Optical Packet Switching. He was one of the initial Optical Engineers of Cognet Microsystems, a startup in Los Angeles, where he directed their Integrated Optics and Advanced Optical Packaging activity. Following the acquisition of Cognet Microsystems by Intel Corporation in 2001, Siva joined Intel's Optical Components Division, where he was a key contributor to the design of several 10 Gb/s transmitter and receiver products and received two Intel Divisional Recognition Awards. Dr. Yegnanarayanan is currently a post-doctoral fellow in the Photonics Research Group at Georgia Institute of Technology, where he is working on Silicon Nanophotonics.

Mohammad Soltani received his B.Sc. and M.Sc. degrees in Electrical Engineering from Sharif University of Technology, Tehran, Iran, in 1999 and 2001 respectively. Since January 2002 he has been a Ph.D. student in the electrical engineering program at Georgia Tech. His general research interests are electromagnetics, quantum electronics, quantum optics, and condensed matter physics. His current research is on the design and fabrication of integrated high-Q Silicon microcavities and coupled waveguide-cavities for filtering, biosensing, and nonlinear optics.

Qing Li received his B.Sc. in Electrical Engineering from Tsinghua University (China) in 2006. He moved to U.S. in 2006 and is currently pursuing Ph.D. at Dr. Adibi's group in Georgia Institute of Technology. His research interests include optical device design and fabrication for on-chip application, nonlinear effects inside high-Q microcavity and quantum optics.

Ehsan Shah Hosseini received his B.Sc. in Electrical engineering from Sharif University of Technology (Tehran, Iran) in 2003. He got his M.S. in 2008 and is pursuing his Ph.D. degree at Georgia Institute of Technology in Photonics Research Group.

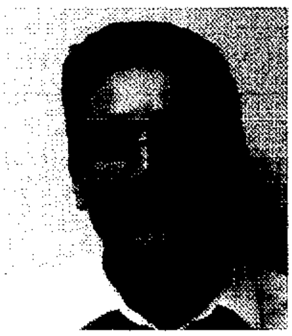

Ali A. Eftekhar has received his B.S. and M.S. in electrical engineering from Sharif University of Technology in 1996 and 1998. Since 2003 he has been a Ph.D. student at the Georgia Institute of Technology. He was an Iranian Physics Olympiad Team member in 1992 in Helsinki, Finland, and also ranked first in national Iranian electrical engineering in 1996. He is cofounder of two companies in 1999 and 2002 in the field of digital broadcasting technology, wireless technology, digital processing, IP telephony and soft switching, where he has served as technical manager and CEO from 1999 to 2003.

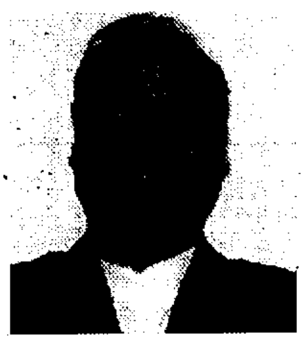

Ali Adibi is a professor in the School of Electrical and Computer Engineering and the director for the center for Advanced Processing-tools for Electromagnetic/acoustics Xtals (APEX) at Georgia Institute of Technology. He received his B.S.E.E. from Shiraz University (Iran) in 1990, and received his M.S.E.E. and Ph.D. degrees from the Georgia Institute of Technology (1994) and the California Institute of Technology (1999), respectively. His Ph.D. research resulted in a breakthrough in persistent holographic storage in photorefractive crystals. His research interests include integrated nanophotonics, reconfigurable integrated photonic structures, lab-on-chip bio and chemical sensing, holographic data storage, phononic crystal structures and acoustic metamaterials, design, characterization, and applications of photonic crystals for chip-scale WDM and biosensing; spectrometers for bio and environmental sensing; high resolution optical imaging for biomedical applications; ultra-dense and ultra-fast optical interconnects; and optical communication and networking. Dr. Adibi has been the conference chair for the "Photonic Crystal Materials and Devices" conference in the Photonic West Meeting since 2001, and the program chair for the "Nanotechnology" program in the Photonic West Meeting since 2002. His is also a member of the editorial board for Springer optical science series, and a topical editor for Applied Optics. He has served as a technical committee member for several conferences organized by IEEE, Optical Society of America (OSA), and The International Society for Optical Engineering (SPIE). He is the recipient of numerous awards including the Presidential Early Career Award for Scientists and Engineers (PECASE, from the White House), the Packard Fellowship (from the David and Lucile Packard Foundation), the NSF CAREER Award (from National Science Foundation), the Technology Achievement Award from the International Society for Optical Engineering (SPIE), the SCEEE Young Faculty Development Award (from the Southeastern Center for Electrical Engineering Education), the NASA Space Act Award (from NASA), SPIE's Young Investigator Award, Outstanding Junior ECE Faculty Award (from Georgia Tech), Howard Ector Outstanding Teacher Award (from Georgia Tech), Richard M. Bass Outstanding Teacher Award (from Georgia Tech), Charles H. Wilts Prize from Caltech (best EE thesis of the year), New Focus Student Award from the Optical Society of America, Top Student (D. J. Lowell) Award from SPIE, and the Oscar P. Cleaver Award from Georgia Tech (Outstanding EE graduate student of the year). He is a senior member of IEEE and a member of OSA and SPIE. He is also the chair of the IEEE LEOS Atlanta Chapter.

enable the realization of ultra-high Q resonators in Si-CMOS compatible substrates, with small mode volumes, suitable for strong light-matter interaction. Specifically, we focus on SOI based substrate for microresonators that are useful in the Si transparency region with wavelengths above 1200 nm, and SiN (Silicon nitride) microresonators on oxidized Si-substrates for microresonators that are useful in the SiN transparency region with wavelengths above 300 nm. Systematic analysis and design of single and coupled-resonator filters is provided. Furthermore, by using a detailed thermal model we demonstrate optimized microresonator structures with improved thermal conductivity that can sustain a high circulating optical intensity at the resonance wavelength, which is particularly useful for nonlinear optics and optical signal processing applications. Finally, we conclude by addressing some of the applications and future prospects of such microresonators in CMOS-compatible substrate technology, including portable multi-purpose bio/chemical sensing systems and reconfigurable optical signal processing modules.

2. HIGH-Q PHOTONIC RESONATORS

2.1. Planar Silicon Resonators

Trends toward the integration of micro photonics and microelectronics in a silicon-on-insulator (SOI) platform have had a lot of progress during the recent years.[16–19] The large refractive index of silicon and its low material absorption at telecommunication wavelengths have enabled the realization of a variety of optical functionalities in micron and submicron scales that are compatible with planar CMOS fabrication. In particular, several recent advances include the demonstrations of high-speed silicon (Si) optical modulators,[20–22] high-speed switches,[22,23] and nonlinear optical Si laser sources based on the stimulated Raman effect.[24,25] Among the different micro-photonic components, microdisk and microring resonators have been actively pursued for chip-scale silicon photonics.[26–29] The high quality factors and small mode volumes that are achievable in micrometer scale devices result in very long photon life time and strong electric field enhancement inside these resonators. These unique properties of such microring/microdisk resonators make them ideal candidates for many applications such as filtering, sensing, delay, and enhancement of light-matter interactions.[30] Moreover, since microdisk is a traveling-wave-resonator (TWR), by appropriate design of waveguide-resonator coupling, a complete 100% transmission of energy from a bus waveguide to the resonator is possible.[31,32] The key challenges in realizing such resonator structures are:

(1) Development of improved fabrication techniques in order to reduce sidewall roughness induced scattering loss in such structures

(2) Engineering of the waveguide-resonator coupling structure to achieve critical coupling.

Here, we address each of the above challenges in detail and provide guidelines to the design of efficient microdisk resonators suitable for chip-scale photonic integration. We also report the largest Q, to our knowledge, which is obtained for such microdisk resonators with integrated input/output coupling structures.

Recently, ultra high Q silicon undercut microdisk resonators were demonstrated, and a detailed study of the many of the non-idealities of the high Q silicon microdisk structures including intrinsic material absorption, Rayleigh scattering from surface roughness due to fabrication imperfections, and surface state absorption was presented.[26–28] This technique has its own challenges with regards to chip-scale integration, namely:

(1) due to the strong phase mismatch between the fiber mode and the Si microdisk mode, energy transfer from the fiber to the microdisk is inefficient, and it is hard to obtain critical coupling, characterized by a complete 100% transmission of energy from a bus waveguide to the resonator and

(2) the fiber is suspended and hence it may be sensitive to mechanical vibration as well as damage and degradation due to environmental effects.[27]

For the goal of integrating several chip-scale functionalities with the microdisk resonator it is essential to use Si-based waveguides for input/output coupling to the microdisk resonator. While undercutting a microdisk resonator is relatively easy, using an undercut waveguide for coupling light to such an undercut resonator is not trivial. For mechanical stability and low-loss performance of the integrated photonic structures it is highly desirable to keep the SiO_2 layer underneath the Si structures intact. In order to assess the impact of the silica substrate, we performed a detailed theoretical study on the effect of oxide substrate on the Q of the microdisk resonator. Two structures were considered for this study, namely a conventional SOI microdisk as shown in Figure 1(a), where the Si layer is completely etched, and a microdisk on Si pedestal as shown in Figure 1(b), where the Si layer is partially etched and as a result a thin Si pedestal layer is left underneath the microdisk. We refer to these two architectures as conventional and pedestal microdisks respectively. There are two main advantages of the pedestal microdisk, namely the silicon pedestal reduces the thermal resistance of the microdisk and also facilitates its integration with active electronics such as MOS transistors and p–n junctions.[20, 22] For instance, nonlinear optical applications in silicon suffer from optical power limitations due to two-photon absorption (TPA) generated free carriers.[16–18] Using the pedestal microdisk architecture, we could potentially integrate a reverse-bias p–n junction with the resonator and sweep the TPA-generated free-carriers away from the microdisk active region.[20, 22]

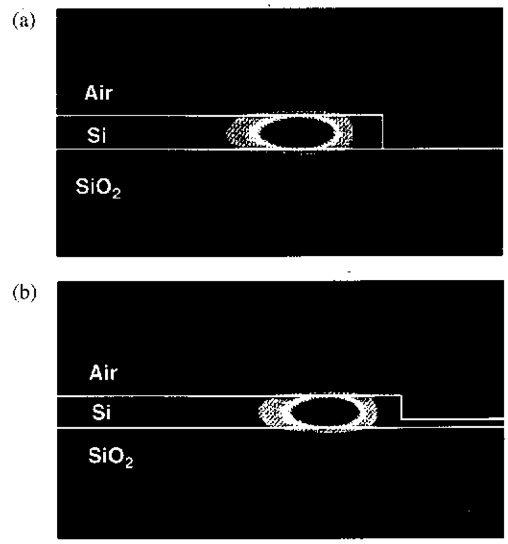

Fig. 1. (a) The cross section of a Si microdisk resonator on oxide substrate, the silicon thickness is 230 nm. (b) The cross section of a pedestal microdisk resonator on oxide substrate; the Si shallow and deep layers have the thicknesses of 60 nm and 225 nm respectively. The energy profile of the fundamental radial TE (electric field predominantly in the plane of the microdisk) mode is shown in the figures. In both cases the disk radius is 20 μm. Reproduced with permission from [35], M. Soltani et al., *Opt. Express* 15, 4694 (**2007**). © 2007, Optical Society of America.

In the simulations of the structures in Figures 1(a and b), we used the finite-element method (FEM) with incorporation of a perfectly matched layer (PML) absorbing boundary condition. The simulation for a microdisk with a Si of thickness 230 nm and a radius 10 μm resulted in a radiation $Q > 10.^{10}$ For the pedestal microdisk, similar results were obtained. Therefore, we conclude that the ultimate limit on the achievable Q is limited mostly by the fabrication limitation and other non-idealities in the device and not by the radiation into the SiO_2 layer. As investigated in,[27, 28] the major non-idealities are:

(1) two-photon absorption assisted free-carrier generation,
(2) surface absorption due to the simultaneous presence of sidewall roughness and surface electronic states, and
(3) thermal resistance. Thus, our theoretical results suggest that this high Q's obtained for undercut microdisk structures,[26–28] should be achievable in the microdisk-on-oxide structures (without undercutting).

To investigate this observation experimentally, we fabricated a series of microdisk resonators with 20 μm radius on a SOI wafer.

2.1.1. Fabrication Of High-Q Cavities

A typical microdisk resonator structure is fabricated on SOI with device thickness of 220–250 nm and buried oxide (BOX) thickness of 3 μm. Fabrication steps begin with growing a 60 nm thermal oxide on SOI wafer as a hardmask. An E-beam resist (ZEP-520A) with a thickness of 350 nm is spin coated on the wafer. Then, the structure pattern is transferred onto the wafer using a JEOL-9300 E-beam lithography system. In order to define the structure, a two-step etching process is used. The first step is to etch the hardmask with $CF_4/CHF_3/Ar$ gases (3/1/1 ratios) in an inductively coupled plasma (ICP) etching system. Then, the resist left on top of the structure is removed and therefore an oxide layer is left on top of the structure as a hardmask. The final step is to etch the silicon with Cl_2 in the ICP chamber. The resulting structure, as shown in Figures 2(a–c), is a microdisk with radius of 20 μm, coupled to a ridge waveguide with width 550 nm with a 220 nm gap between the microdisk and the waveguide. The measured sidewall angle was more than 85 degrees. The thickness of Si is 225 nm, and a thin layer of thermal oxide is left on top of the structure.

Figure 3 shows the spectrum of the microdisk resonator shown in Figure 2. The measurement was done using a swept-wavelength test setup. A tunable laser operating in the continuous sweep mode was used as the source. A fiber polarization controller followed by a polarizer was used to control the input polarization state to the device. We used a standard objective lens for coupling into and out of the device. Conventional adiabatic tapering was used at the waveguide input facet in order to reduce the insertion loss. The output light from the device was spatially filtered using an aperture stop to remove stray light, before being converted to an electrical signal in a photoreceiver and interfaced to computer through a data acquisition (DAQ) card. As can be seen from Figure 3(a), several different resonant modes with Q's ranging from 1.5×10^5 up to 2.0×10^6 were observed, corresponding to different radial mode orders.

Pedestal microdisks, such as the one shown in Figure 1(b), were also fabricated and characterized. The disk radius and the input/output coupling waveguide are identical to the microdisk shown in Figure 2, with the only difference being that by controlling the etching depth of the microdisk, we leave a thin pedestal layer of silicon under the resonator. Figure 4 shows the SEM cross section of this device. From the SEM measurement, the thickness of the thin pedestal layer, after the fabrication, was in the range of 60 nm–66 nm. As can be seen from this figure, trenching is observed at the interface of the device and the pedestal layer. This trench formation, which is typical in Cl_2 chemistry based plasma etching of silicon,[33] can be further reduced by more optimization of the Si etch recipe.

Figure 5(a) shows the spectrum of this pedestal microdisk. We observe that the spectrum exhibits less resonance features compared to the resonance spectrum of the conventional microdisk shown in Figure 3(a). We ascribe this to the fact that the thin pedestal layer increases the radiation losses for higher order radial modes, thereby reducing the Q of these modes. Figure 5(b) shows the resonance spectrum of the 2nd order radial mode. As it can be seen from this figure, resonance splitting is observed for this mode. Lorentzian fitting with taking resonance splitting into account was applied, and an intrinsic (unloaded) Q of about 3.0×10^6, was achieved in this pedestal microdisk architecture. We anticipate this pedestal microdisk to be an enabling device platform suitable for integration with p–n junctions and other active electronic components with great potential to be used for modulation and switching applications.

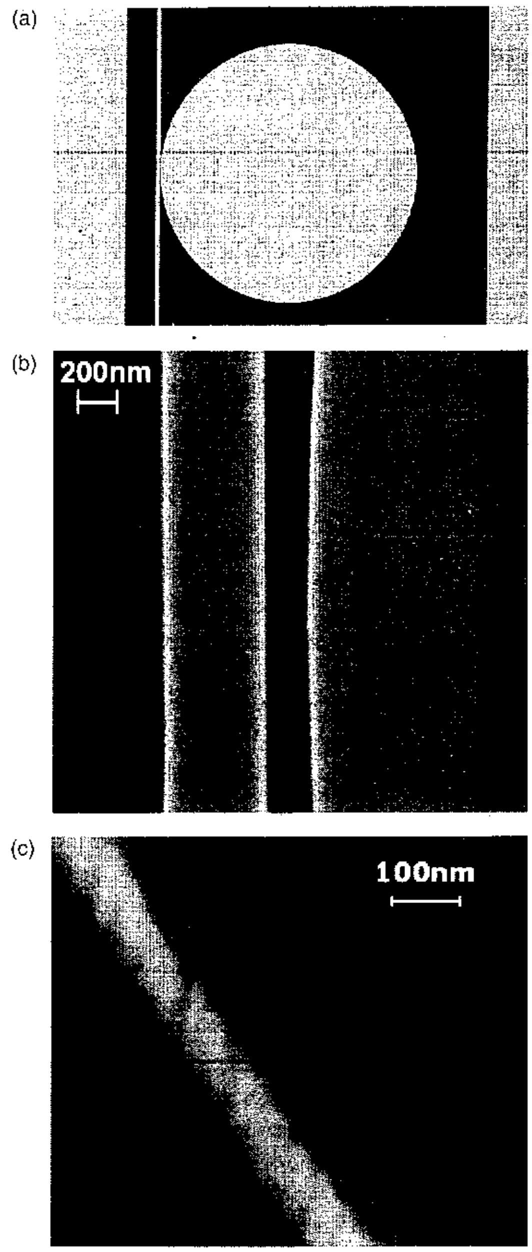

Fig. 2. (a) SEM micrograph of a Si microdisk resonator side-coupled to a waveguide fabricated in Adibi's group at Georgia Tech: the disk radius is 20 μm and its thickness is 225 nm. The waveguide width in is 550 nm. The gap between the disk and the waveguide is 220 nm. (b) A closer view of the structure at the waveguide-cavity coupling region. (c) Sidewall of the microdisk captured at an azimuth angle of 30° and a sample tilt angle 30°. Reproduced with permission from [35], M. Soltani et al., *Opt. Express* 15, 4694 (**2007**). © 2007, Optical Society of America.

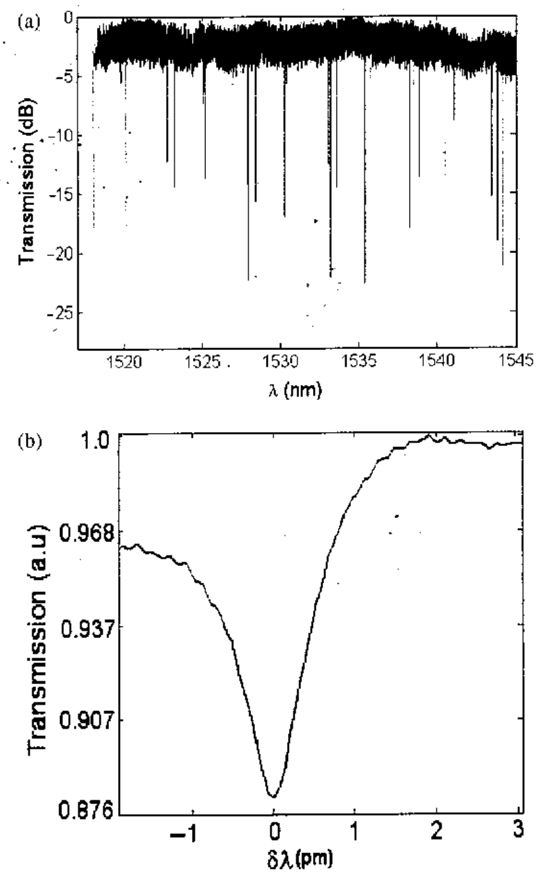

Fig. 3. (a) Spectrum of the microdisk resonator shown in Figure 2 for TE polarization. (b) An ultra-high $Q = 2 \times 10^6$ was observed at $\lambda = 1520.188$ nm. From the simulation results, this resonance wavelength corresponds to a 2nd radial order mode with an FSR of 5.1 nm. Reproduced with permission from [35], M. Soltani et al., *Opt. Express* 15, 4694 (**2007**). © 2007, Optical Society of America.

2.1.2. *Efficient Coupling to Photonic Resonators*

For high-Q resonators, efficient coupling of the light into the resonator is an important task in realizing a functional system. Depending on the application, undercoupled, overcoupled, or critically coupled resonators are needed, and in all cases, it is important to have a systematic way to exactly control the amount of coupling between the resonator mode and the waveguide carrying the light to/from the resonator.

In a TWR-waveguide coupling structure, coupling $Q(Q_c)$ depends on the cavity mode volume, coupling interaction length, and effective mode index matching between the waveguide and TWR modes.[34] Larger cavity mode volumes increase Q_c, while larger coupling interaction lengths result in reduction of Q_c. However, the effect of the mode index mismatch between the disk and the waveguide on Q_c is dramatic, and is illustrated below. Since the microdisk resonator is a TWR structure, as discussed in Ref. [35], we can ascribe to each microdisk mode, a phase and an associated effective mode index. In the case of the large index mismatch between the microdisk and the

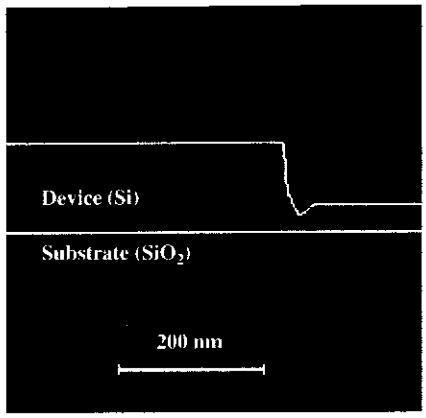

Fig. 4. SEM cross section of the pedestal type structure captured at a sample tilt angle 30°. The microdisk radius and thickness are 20 μm and 225 nm respectively, and the thickness of the shallow layer is 65 nm. Reproduced with permission from [35], M. Soltani et al., *Opt. Express* 15, 4694 (**2007**). © 2007, Optical Society of America.

waveguide, coupling is strongly reduced, so much so that even bringing the waveguide very close to the cavity does not significantly alter their coupling. Moreover, putting the waveguide and resonator too close to each other results in

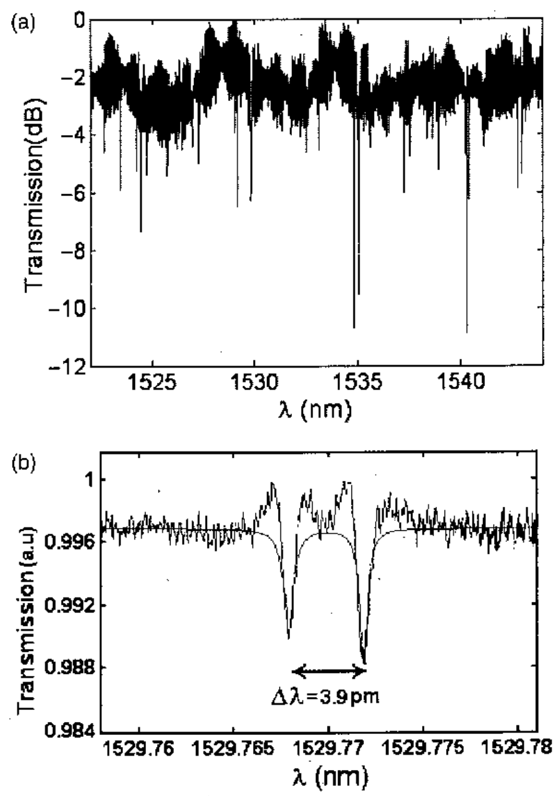

Fig. 5. (a) Spectrum of a pedestal microdisk resonator coupled to a waveguide for TE polarization. (b) Spectrum of the 2nd order radial mode; mode-splitting due to the coupling of CW and CCW is observed. The disk radius and the input/output coupling waveguide are identical to the conventional microdisk shown in Figure 2. Reproduced with permission from [35], M. Soltani et al., *Opt. Express* 15, 4694 (**2007**). © 2007, Optical Society of America.

strong perturbation of the cavity structure,[37] resulting in additional loss and the resultant degradation of the Q.

In order to illustrate this coupling and index matching issue, using the coupled mode analysis,[36] we consider the microdisk and waveguide whose dimensions are given in Figure 2. Figure 6(a) shows the effective mode index for different radial modes of this microdisk. Also shown in Figure 6(a) is the fundamental TE mode of the waveguide. As it can be seen, the 3rd order radial microdisk mode has an effective index that is closer to that of the waveguide. Hence, we expect this mode to be better phase matched to the waveguide mode, thereby resulting in a strong coupling. Figure 6(b) shows the calculated coupling $Q(Q_c)$ for different waveguide-cavity gaps, based on a coupled-mode formalism and using the FEM calculated field profiles for the disk and waveguide. As it can be seen from Figure 6(b), the 3rd order radial mode has a lower value of Q_c, thereby confirming the prediction of better waveguide-cavity coupling, i.e. closer to critical coupling, than the lower order modes based on the phase-mismatch obtained from effective indices in Figure 6(a). For a gap of 220 nm, for the 1st order radial mode, Q_c was

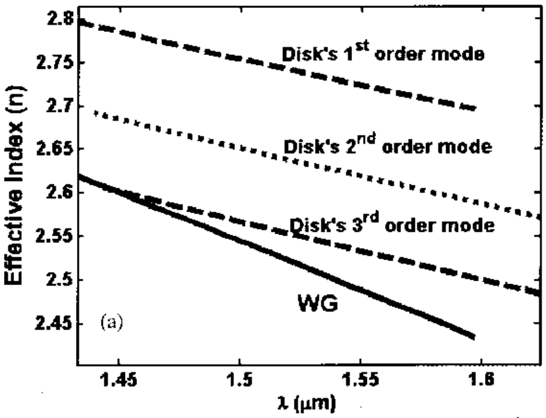

(b)

$Q_c/10^6$ (λ~1520)

Mode \ Gap	150 nm	220 nm
	10	40
	3	15
	1.8	7

Fig. 6. (a) Comparison of the effective indices of the traveling TE modes of the microdisk resonator shown in Figure 2 for different radial mode orders with that for the waveguide. The dimension of the disk radius and the waveguide is given in the caption of Figure 2. (b) Q_c for different gaps between the waveguide and the microdisk calculated using coupled mode theory. Reproduced with permission from [35], M. Soltani et al., *Opt. Express* 15, 4694 (**2007**). © 2007, Optical Society of America.

calculated to be 40×10^6. Therefore, it is reasonable not to be critically coupled to the fundamental mode for this waveguide-resonator geometry parameters. The same argument applies for the 2nd and 3rd order modes. However, for the gap of 150 nm, the values of Q_c vary in the range of $1 \times 10^6 - 6 \times 10^6$ and are closer to what we may achieve for the intrinsic Q of the cavity, thereby ensuring we are closer to critical coupling. The results shown in Figure 6 clearly demonstrate the importance of the phase-matching of the waveguide and the cavity modes for achieving good coupling. This fact was experimentally confirmed by achieving critical coupling for the 4th order radial mode which is closely index matched to the waveguide, as shown in Figure 7. As it can be seen in this figure, almost 99% of the energy is transferred from the waveguide to the cavity at resonance. From this spectrum an unloaded $Q \sim 0.7 \times 10^6$ was extracted.

2.1.3. Thermal Stability

High Q and low electromagnetic mode volume of planar Si microresonators can build up a strong electromagnetic field inside them, even at low optical powers. As a result, strong interaction of electromagnetic field with the material (Si in this case) can occur inside the resonator.[28,38] This may proceed to nonlinear effects such as two photons absorption (TPA) which accordingly generates a large number of free carriers (FC) inside the resonator.[28] The effect of these free carriers on the properties of the microresonators are

(i) Mode energy of the resonator can be absorbed and converted into heat energy which accordingly degrades the Q:
(ii) The resonator temperature rises up due to the generated heat which consequently changes the refractive index of the resonator in the positive direction. Hence, a thermally induced linewidth broadening occurs in the spectrum of the resonator;[28,38,39]

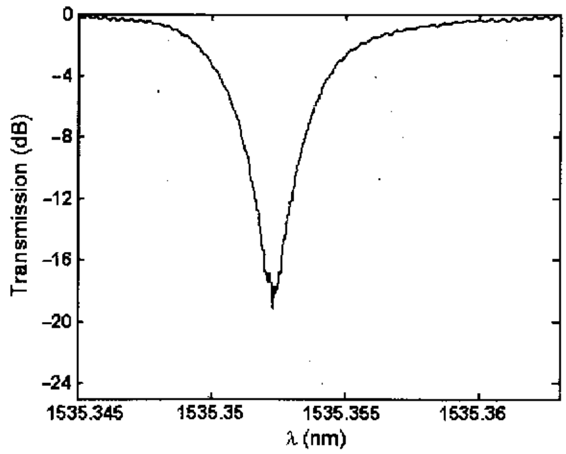

Fig. 7. Experimental observation of critical coupling for the 4th order radial mode for the conventional microdisk shown in Figure 2. The measured unloaded Q is about 0.7×10^6. Reproduced with permission from [35], M. Soltani et al., *Opt. Express* 15, 4694 (**2007**). © 2007, Optical Society of America.

(iii) Refractive index of the resonator changes in the negative direction due to the free carrier dispersion effect,[28] thereby, a blue shift in the resonance frequency of the resonator occurs.

Hence, increasing the optical power, in a lot of high Q resonator applications, can degrade the performance and sensitivity of the device due to the linewidth broadening. Therefore, the structure of the resonator should be functionalized or modified to suppress or at least minimize these non-idealities on the spectral response of the resonator.[40]

In order to first observe the thermal non-idealities at high powers in Si microresonators, we fabricated ultra high Q microdisk and characterized its spectrum at different levels of input power. In Figure 8(a) the scanning electron microscope (SEM) image of a Si microdisk resonator with radius 20 μm and thickness 250 nm, coupled to a waveguide with a width of 550 nm is shown. A shallow Si pedestal layer with a thickness of about 50 nm is at the interface between the oxide layer and the microdisk.

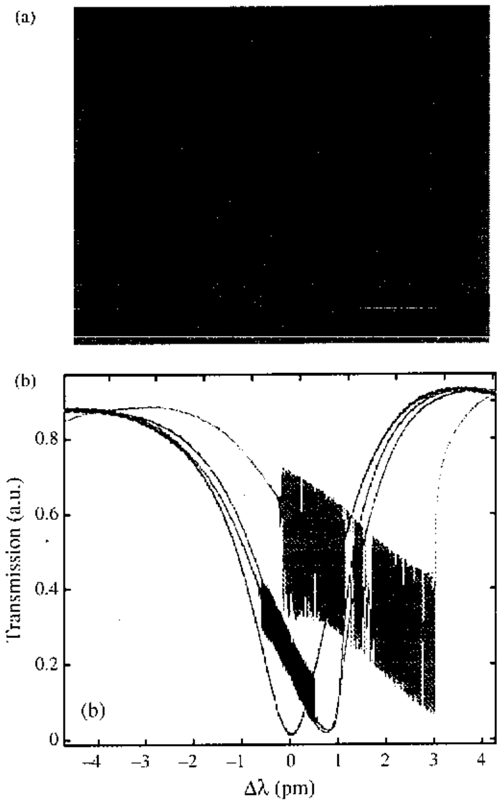

Fig. 8. (a) SEM image of a Si microdisk resonator with radius 20 μm and thickness 250 nm coupled to a waveguide with the width 550 nm. (b) The resonance spectrum of one of the microdisk modes at the critical coupling regime for different values of input optical power. The blue curve and the orange curve correspond to the lowest power and the highest power, respectively. By increasing the power, thermally-induced linewidth broadening as well as oscillation appears in the spectrum. The unloaded Q of this resonance mode is $Q \sim 1.2 \times 10^6$. Reproduced with permission from [40]. M. Soltani et al., *Opt. Express* 15, 17305 (**2007**). © 2007, Optical Society of America.

The spacing between the waveguide and the resonator is 200 nm in order to achieve critical coupling between the waveguide mode and the resonator mode. Figure 8(b) shows the spectrum of one of the resonance modes of this microdisk measured at different levels of input optical power in the waveguide. As seen from Figure 8(b), the broadening of the spectrum is observed at higher powers, where the spectrum deviates from a Lorentzian shape and becomes asymmetric. As shown in Figure 8(b), by orange curve, further increase in the optical power results in thermal-FC oscillations. This is a cycling dynamic between the blue shifting of the resonance due to TPA-induced FC generation, and red shifting of the resonance due to the temperature rise as a consequence of FC absorption and heating generation. Thorough discussion of the heating for a traveling wave resonator (TWR) such as a microdisk that is coupled to a waveguide is available in several works.[39]

At steady state, the heat generated in the microresonator through optical (FC) absorption is completely balanced by the heat flux leaving the cavity through the "effective" thermal conductivity of the microresonator to the surrounding thermal ambient ("bath"). This results in the usual thermal bistable response for the cavity spectral response at high optical power. Following a detailed analysis of our Si microdisk resonator we found the following trend, for high Q microresonators, larger thermal conductivities (K) enables larger optical power (P) to be coupled into the resonator while no bistability and less broadening is observed in the resonance spectrum.[40] Moreover, for ultra-high Q cavities, the threshold power scales linearly as the thermal conductivity and an increase in thermal conductivity directly translates into a higher coupled power into the cavity, thereby enabling high-power and potentially nonlinear applications.

In order to perform a quantitative comparison of the effect of the various microresonator structural parameters, on the effective thermal conductivity, we solved the steady-state heat Eq. (1),

$$-\nabla \cdot (K \nabla T) = Q_{\text{th}} \tag{1}$$

in which, K is the thermal conductivity of different materials used in the structures, and Q_{th} is the rate of heat energy generated in the structure. Considering the axial symmetry of the structure and simplifying the heat equation and also using heat generation rate in Si microdisk, Q_{th} is proportional to the electric mode energy (proportional to $|E|^2$, with E being the electric field inside the resonator) of the microdisk, we arrive at the formalism in Eq. (2),

$$-\frac{1}{r}\frac{\partial}{\partial r}\left(rK\frac{\partial T}{\partial r}\right) - \frac{\partial}{\partial z}\left(k\frac{\partial T}{\partial z}\right) = Q_{\text{th}} \tag{2}$$

which can be solved for a given microdisk resonator to find the temperature distribution inside the structure. We

REVIEW

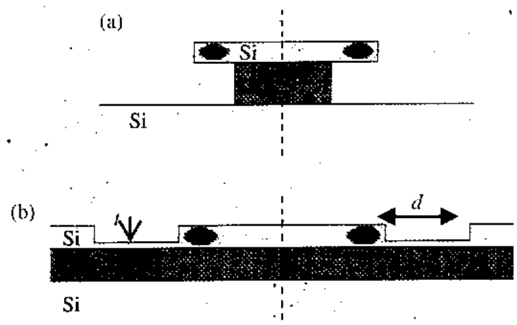

Fig. 9. (a) Cross section of an undercut Si microdisk resonator held by an oxide micropost on a Si bulk layer. (b) Cross section of a Si microdisk resonator on an oxide substrate. A shallow Si pedestal layer with thickness t is at the interface between the microdisk and the oxide layer. The etched region that separate the disk perimeter from the surrounding top silicon layer is d. In both (a) and (b) the cross-section of the generated heat energy, which has a distribution proportional to that of the electromagnetic mode energy of the resonator, is shown. Reproduced with permission from [40], M. Soltani et al., *Opt. Express* 15, 17305 (**2007**). © 2007, Optical Society of America.

use an in-house finite element code for solving Eq. (2) in the COMSOL environment.

In order to assess the role of SiO_2 substrate and the shallow Si pedestal layer on the thermal conductivity of the microdisk resonator the following structures were considered for the analysis: (1) an undercut microdisk held by an oxide micropost (shown in Fig. 9(a)), and (2) a Si pedestal disk with the thicknesses of the pedestal layer (t) which is in general covered by either air or an oxide cladding (shown in Fig. 9(b)).

For the undercut disk, the radius and height of the underneath micropost oxide were 17 μm and 1 μm, respectively. Using a finite element technique as discussed in Ref. [35] the electromagnetic mode profile of the structure is obtained. Here, we focus on the fundamental radial mode of the disk, although the final results for different modes regarding the thermal properties are similar. After finding the mode of the resonator, the generated heat energy that has a distribution proportional with the energy mode profile of the microdisk is incorporated into Eq. (2). Using a finite element method and applying the cylindrical symmetry conditions in the structure, the steady state temperature distributions of these structures can be obtained by solving Eq. (2). Figure 10(a) shows the temperature distribution for a typical pedestal microdisk with the dimensions given in the figure captions. As can be seen from Figure 10(a), the peak temperature location coincides with the position of the maximum concentration of the electromagnetic energy, which is in the vicinity of the disk edge. A similar simulation can be performed for the undercut microdisk shown in Figure 9(a). The results of these simulations show that the maximum temperature occurs when the electric field energy of the resonator mode is maximum (i.e., in the vicinity of the disk edge).

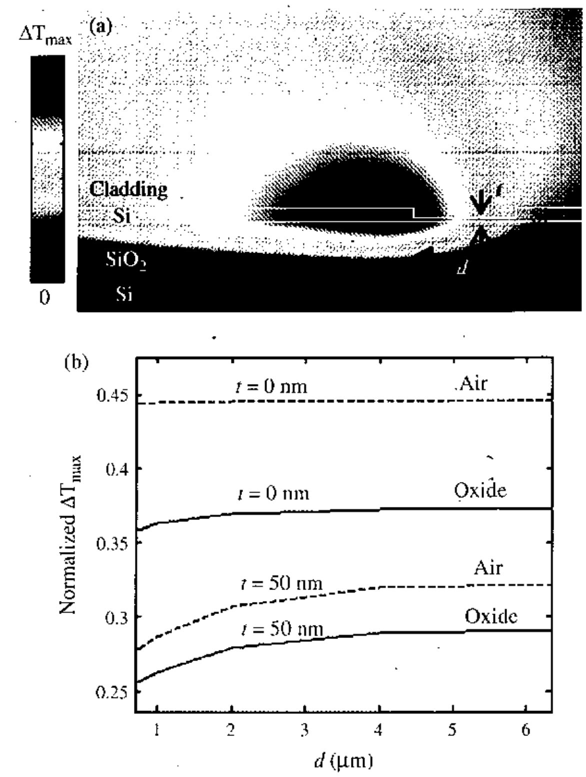

Fig. 10. (a) Cross section of the temperature distribution in a Si pedestal microdisk resonator on substrate; the disk radius and thickness are 20 μm and 250 nm, the Si pedestal thickness is 50 nm; and the oxide substrate thickness is 1 μm. (b) The normalized peak temperature of the pedestal microdisk resonator with air and oxide claddings are also shown with dash and solid lines, respectively, for different value of d, which is the distance between the disk edge and the surrounding silicon layer. The temperatures are normalized to the peak temperature of the undercut microdisk under similar energy inside the microdisk resonators. Reproduced with permission from [40], M. Soltani et al., *Opt. Express* 15, 17305 (**2007**). © 2007, Optical Society of America.

Based on the thermal conduction of the two structures shown in Figure 9, it is expected that the undercut microdisk structure has the optical highest temperature rise at a given input power. To investigate this fact more quantitatively, we calculated the maximum temperature for both structures by solving Eq. (10). Figure 10(b) shows the normalized peak temperatures rise of the pedestal disk with air cladding and oxide cladding for pedestal thicknesses of $t = 0$ nm and $t = 50$ nm, respectively. As shown in this figure, the temperatures are normalized to the peak temperature rise of the undercut microdisk. These results show a dramatic reduction (over 3×) in the peak temperature (proportional to the thermal resistance), by using the pedestal microdisk architecture in comparison with undercut microdisk. Thus, the presence of the oxide layer is very important, especially for high power applications of the microdisk resonator. For narrower micropost radii, the simulations confirmed that the peak temperature was even larger for the undercut microdisk. In addition, our results show that the Si pedestal layer has a major role in improving the overall thermal conductivity of the structure. In fact, it is observed from Figure 10(b) that the pedestal disk with even an air cladding has lower peak temperature when compared with the disk without the pedestal layer but covered with oxide cladding. Finally, the addition of the overall oxide cladding further improves the thermal conductivity as expected. Thus, depending on the application and the level of power used in the actual experiments involving the Si microresonators, one can have different levels thermal conductivity improvements by adding different layers (i.e., underneath SiO_2 layer, pedestal layer, and the oxide cladding layer) to the resonator. Our simulations were for different pedestal widths (d), which is the distance between the disk edge and the surrounding Si region. It is observed that the peak temperature rise increases with increasing d and eventually saturates at large d, due to the competition with the underneath substrate Si/oxide effects.

Thus, the thermal properties of high Q Si microresonators highly depend on the resonator structure and by preserving the oxide layer underneath the Si in a microdisk resonator we can considerably improve the thermal conductivity of the structure without sacrificing Q. The presence of a shallow Si pedestal layer at the interface between the microdisk and the oxide layer further improves the thermal conductivity of the resonator by thermally connecting the Si disk to the surrounding Si region, thereby, suppressing the thermal instability issues at high optical powers while preserving the ultra high Q property of the resonator.

2.1.4. *Coupled-Resonator Filters*

The ability to realize ultra-compact microresonators with high-Q enables their use for optical filters using coupled-resonator architectures.[41,42] For sufficient large-order cascaded coupled-resonators, the large mode mismatch at the input/output ports between the bus waveguide and a coupled resonator section, results in severe intensity and group delay ripples in the passband. Here, we report our recent work in developing a simpler approach for designing an efficient and large bandwidth filter consisting of coupled racetrack resonators made of single-mode waveguides with the same dimension as the coupling bus waveguide.[43] In this design approach, we benefit from two advantages, namely,

(1) the filter design parameters are obtained with less computation effort, and

(2) the insertion loss introduced by the coupling between the waveguide and the resonators is negligible.

In addition, the coupling-induced resonance frequency shifts (CIFS) is another important issue in coupled-resonators filters. Depending on the resonators geometry and their coupling scheme, CIFS can strongly distort the filter response.[44,45] We have included this issue in our design and using our compensation techniques we have been able to suppress this effect. Our goal is to design an add-drop flat-band filter with a large bandwidth (3 dB bandwidth ~ 3.3nm) and a large FSR (~18nm) to achieve similar performances as demonstrated in the previous work.[46,47] For the demonstration purpose we focus on the design and demonstration of a 3rd-order filter as shown in Figure 11(a). All the designs, simulations and measurements are for the TE polarization, i.e., electric field is predominantly in the plane of the structure. From the FSR consideration, the perimeter of individual racetrack resonators that constitute the 3rd-order filter must be around 31 μm, assuming a group index of 4.22 for a single-mode ridge waveguide with dimension of 500 nm wide and 215 nm high above the oxide. From the bandwidth and the FSR considered above, the power coupling coefficient κ^2 between the resonator and waveguide and the mutual power coupling coefficient κ_m^2 between the resonators (see Fig. 11(a)) are required to be 0.82 and 0.18, respectively (κ, κ_m itself is the field coupling coefficient), which are extracted from the rigorous transfer matrix analysis.[48] Note that for large bandwidth filter design, where stronger coupling between the waveguide

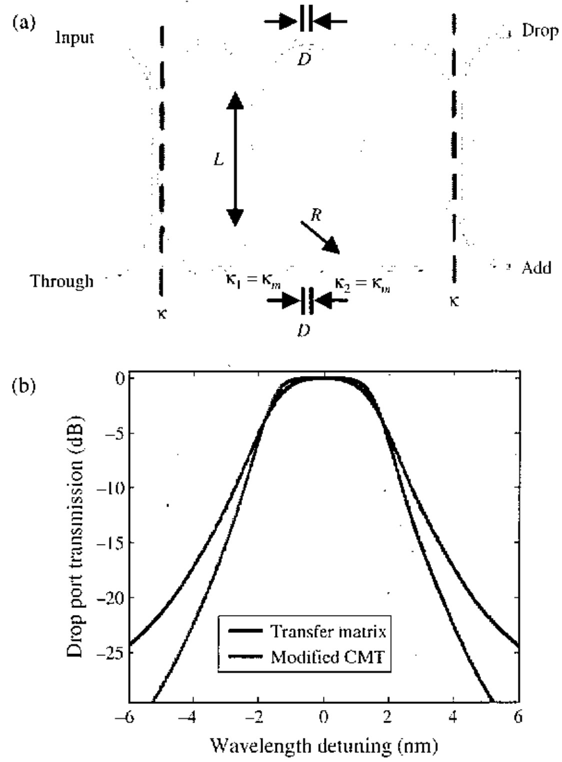

Fig. 11. (a) Schematic of a 3rd-order filter made of three racetrack resonators; the length of the center resonator is adjustable, as shown by the length parameter D, to compensate the CIFS effect; the two vertical dash lines are the symmetry axis of the waveguide-resonator coupling structure, as proposed in the symmetric-coupling scheme[32] (b) drop port transmission response of the 3rd-order filter given by transfer matrix analysis and the modified CMT, respectively. Reproduced with permission from [43], Q. Li et al., *Opt. Express* 17, 2247 (**2009**). © 2009, Optical Society of America.

and resonators is required, the well-known narrow-band filter synthesis based on the first-order temporal coupled-mode theory (CMT) technique fails to generate accurate design parameters[49] (for example, for 3rd-order narrow-band filters, the flat-band condition requires that $\kappa_m^2/\kappa^4 = 1/8$,[49,50] which is different from what we have calculated above). The reason for this discrepancy lies in the fact that in temporal CMT, the resonator field energy is represented by a normalized parameter so that the resonator energy uniformly scales with any change in that parameter.[36,49,51] However, when the resonator is strongly coupled to another resonator or waveguide, this assumption is no longer valid. In fact, because of the strong perturbation, the energy (power) distribution in the resonator at the coupling region differs from the other parts of the resonator. We find that for flat-band filter design, by introducing an equivalent length instead of the resonator perimeter for the end resonators, which are strongly coupled to bus waveguide, the CMT still works quite well.[43] Figure 11(b) shows the simulated transmission response at the drop port using the transfer matrix analysis.[48] Also, the ideal 3rd-order flat-band (Butterworth) response predicted by the modified CMT is plotted, assuming a coupling quality factor (Q) of 470 between the bus waveguide and the first resonator in the filter. As shown in Figure 11(b), good agreement is observed between the two methods in the passband. However, in the out-of-band region, the modified CMT gives a larger out-of-band rejection ratio. The difference is ascribed to the fact that CMT only considers one FSR in the analysis and the contributions from neighboring FSRs are not accounted, which can limit the rejection ratio especially in the small finesse filters.

In the compensation of CIFS, we use the symmetric coupling scheme, as we proposed in Ref. [45], which is graphically shown in Figure 11(a), where the bus waveguide-resonator coupling geometry is symmetric along the wave propagation direction instead of the conventional straight bus waveguide coupling. In this case, the coupling structure is phase-matched and only the second-order coupling effect is present.[45]

Based on the filter parameters regarding the FSR and bandwidth and also the compactness of the structure, the following parameters are specified according to the filter requirements and simulations: the bending radius of the resonators is chosen to be 3 μm, the interaction coupling length L is found to be 7 μm, and the four gaps as shown in Figure 11(a) are found to be (45 nm, 120 nm, 120 nm, 45 nm), respectively. The CIFS calculation shows that the resonance of the middle resonator is about 200 GHz larger than that of the other two side resonators, where the coupling to the bus waveguide is strong.[45] We accordingly compensate this, by increasing the middle resonator's perimeter by adding a length D as shown in Figure 11(a) to be 14 nm.

The filter is fabricated on a SOI wafer with 215 nm lightly p-doped silicon on top of a 1 μm buried oxide layer. The device is patterned using a dilute hydrogen silsesquioxane (HSQ) negative electron resist with a thickness of 110 nm in a JBX-9300FS electron beam lithography (EBL) system. After developing the pattern, it is etched in an inductively-coupled plasma etching system with a Cl_2 chemistry. Figure 12 shows scanning-electron micrographs (SEM) of the fabricated device. Figure 13(a) shows the measured TE-polarized transmission spectrum of the filter shown in Figure 12. The data shows that our filter has a 3-dB bandwidth of about 3.3 nm and a FSR of about 18 nm. The out-of-band rejection is more than 18 dB at the drop port, and the crosstalk is less than −12 dB at the through port. The small fluctuations seen in Figure 13 is mainly from the remaining Fabry-Perot effect, which arises from reflections at the waveguide/air interface at the cleaved facets. To evaluate the performance of the individual resonators that constitute the filter, a single resonator coupled to a waveguide is fabricated on the same chip. The measured intrinsic Q is found to be between 30,000 ~ 40,000. Such a relatively high intrinsic Q gives a theoretical drop loss of less than 0.5 dB for the 3rd-order filter. The actual insertion loss is inferred by comparing Fabry-Perot response at the drop and through port and this measured insertion loss agrees quite well with the theoretical prediction, that is, less than 0.5 dB. The experimental data is also compared with the simulation results over one FSR, as shown in Figure 13(b). The limited extinction (12 dB) of the through port is because of the deviation of the mutual power coupling coefficients, i.e., κ_1^2 and κ_2^2 as shown in Figure 11(a), from the designed value κ_m^2. This deviation is caused by the fabrication errors which are on the order of 5–10 nm in the EBL step and the subsequent developing step. By fitting the experimental data with temporal CMT simulation, we are able to extract the actual mutual power coupling coefficients ($\kappa_1^2 = 0.9\,\kappa_m^2$ and $\kappa_1^2 = 1.1\kappa_m^2$). Moreover, the almost symmetric response of the through port indicates that the CIFS is largely compensated by our CIFS compensation technique. The out-of-band rejection at the drop port is limited to 18 dB while the designed value is more than 25 dB (see Fig. 11(a)). We ascribe this

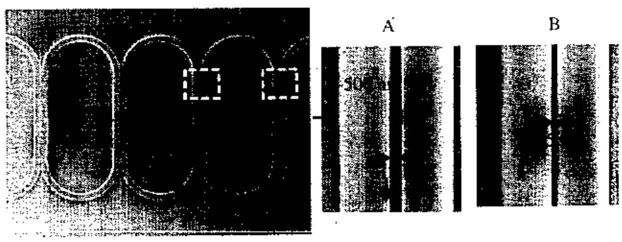

Fig. 12. Scanning-electron micrographs of the fabricated 3rd-order filter made of three coupled racetrack resonators. Each individual resonator is made of a waveguide with a 500 nm width and a 215 nm height and an outer bending radius of 3 μm. The figures at the right show a portion of the coupling regions with the gaps as specified. Reproduced with permission from [43], Q. Li et al., *Opt. Express* 17, 2247 (**2009**). © 2009, Optical Society of America.

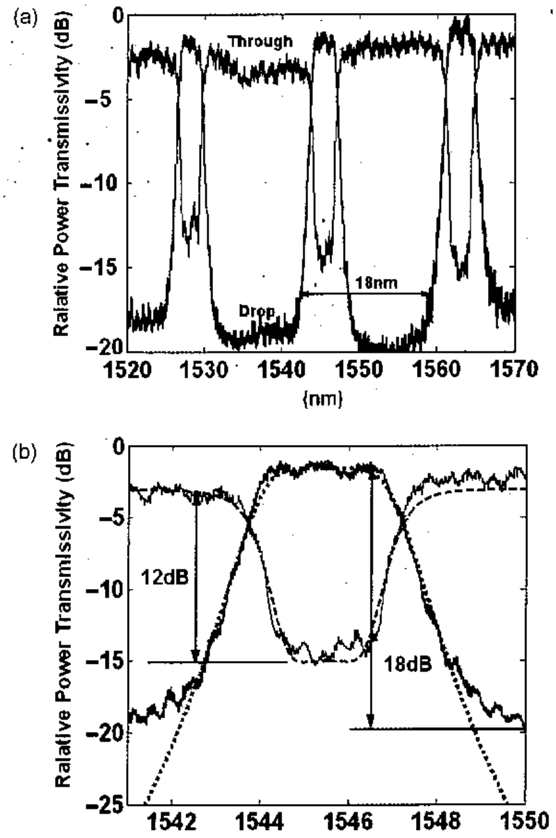

Fig. 13. (a) Experimental responses of the drop and through ports of the 3rd-order filter shown in Figure 2(a); (b) Experimental (solid) and simulated (dashed) responses of the filter around 1550 nm showing one FSR. Reproduced with permission from [43], Q. Li et al., *Opt. Express* 17, 2247 (**2009**). © 2009, Optical Society of America.

to the sensitivity of our setup and also the observed strong light scattering from the shallow 1 μm buried oxide layer. We expect to obtain an improvement in the out-of-band rejection by increasing the thickness of the buried oxide layer.

The design approach presented here for coupled-resonator filters, enables a chip-scale filter with a large bandwidth (~3.3 nm), a large FSR (~18 nm), and a very low insertion loss (<0.5 dB), in a compact form-factor (<0.0004 mm^2) made of three coupled racetrack resonators on a SOI platform. Such a coupled-resonator filter is a key building block component for the future chip-scale wavelength division multiplexing and optical signal processing applications.

2.1.5. Near-Field Characterization

In most applications of high Q microresonators, the interaction of the optical modes of the microresonator and an external perturbation at the proximity of the resonator is utilized. This makes it essential to know the near field profile of the cavity mode. For this purpose, we have developed a technique for sub-wavelength near-field imaging of the optical modes in microdisk cavities by measuring the effect of a small perturbation (caused by the scanning AFM tip) on the transmission amplitude and phase of the coupled waveguide microdisk cavity. Different effect of the perturbation caused by the AFM tip on the optical modes in the cavity (i.e., loss, resonance shift, mode coupling) and their effect in the transmission amplitude and phase of the system are studied. The experimental results confirm that the primary factor that contributes to the change in the transmission amplitude and phase is the shift in the resonance wavelength of the cavity caused by the perturbation.

While conventional Near-field scanning optical microscopy (NSOM) techniques are based on the coupling of light from the evanescent field of the optical modes to the collecting filer, through the NSOM sub-wavelength aperture probe, they suffer from some limitations,

(i) spatial resolution of the technique is limited by the relatively large size of the aperture which is required to couple sufficient power to the NSOM probe, and

(ii) the large NSOM probe significantly perturbs the optical modes of the cavity significantly and makes it impossible to measure the actual mode profile of the resonant mode of the cavity.

As an alternative technique, the aperture-less NSOM techniques have been proposed, that use the small NSOM tip as a sub-wavelength perturbation in the near-field region of the desired mode and collecting the far-field scattered light.[52] Aperture-less NSOM technique has also been used to characterize the mode profile of the guided mode in an optical waveguide by measuring the transmission loss of the waveguide instead of the scattered light power.[53]

Here, we present an alternative technique for the characterization of the mode profile of high-Q microresonators based on the effect of small perturbations on the transmission amplitude and phase of a coupled waveguide-cavity system.[54,55] The small perturbation in this case is a small AFM tip that scans the surface of the cavity, as shown in Figure 14, and is modeled by a small dielectric perturbation on the surface of the cavity. The perturbation of the cavity mode caused by the tip affects the cavity in three different ways namely;

(1) Increasing the microdisk cavity loss due to the scattering and absorption through the perturbation.

(2) Shifting the resonance wavelength of the cavity due to the small refractive index change,

(3) Coupling the degenerate clockwise and counterclockwise modes inside the microdisk cavity that leads to mode splitting.[26]

Although all of these factors affect the coupled waveguide-cavity transmission amplitude and phase simultaneously, and their effects scale with the cavity mode field intensity at the perturbation position, nevertheless, their effects are completely different and depend on the cavity quality factor, the waveguide-cavity coupling and the detuning of the

REVIEW

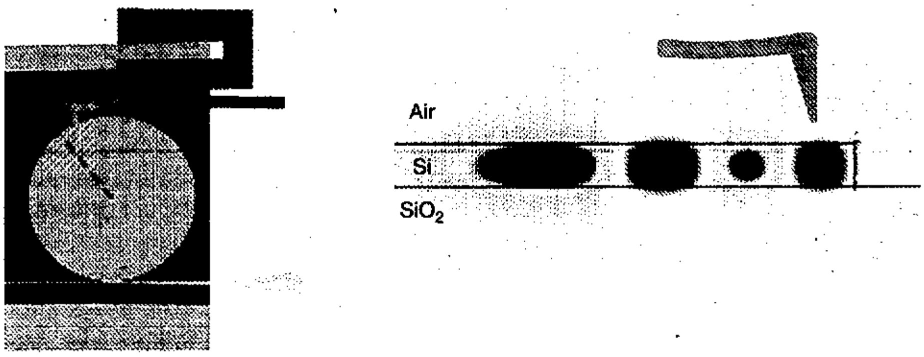

Fig. 14. (left) Schematic of the experimental set up. Light is coupled into and out of the structure through two tapered fibers. A scanning AFM tip is used as a controllable perturbation. (right) The cross section of the electric field profile of a forth order radial mode in a microdisk cavity simulated using finite element method.

input laser wavelength from the resonance wavelength of the unperturbed cavity.

To experimentally investigate the effects of a small perturbation on the optical modes in a microresonator, a microdisk cavity with a diameter of 40 μm is fabricated on an SOI substrate. The thickness of the silicon slab layer is 230 nm. The light is coupled to the microdisk cavity through a waveguide and the cavity to waveguide coupling adjusted to operate close to the critical coupling.[35] Figure 15 shows the transmission of the microdisk cavity for TE polarization (Main components of E field is in the plane of the resonator) in a small wavelength range around the microdisk resonance mode at $\lambda = 1529.71$ nm. The resonant mode of the unperturbed cavity has a loaded Q (i.e., Q after coupling to the waveguide) of 233,000 that correspond to a resonance line width of 6.56 pm. The phase response of the cavity is also shown in Figure 15 and is obtained by heterodyne detection of the output signal. Taking the amplitude and phase information together, we estimate that the cavity is in the under-coupled case where the coupling Q (i.e., $Qc = 796{,}000$) is larger than the intrinsic Q (i.e., $Qi = 329{,}000$) of the cavity. The cavity mode is perturbed by a small AFM tip with a diameter of 20 nm and a tapering angle of 20 degree. The input laser is initially 0.85 pm red shifted with respect to the microdisk cavity resonant mode.

Figure 16 shows the change in the transmission phase and amplitude as the AFM tip scans the surface of the microdisk cavity in the radial direction. The interaction between the AFM tip and the optical mode in the microdisk cavity depends on the electrical field intensity at the tip position. As it can be observed from Figure 16, the resonant mode is a fourth-order radial mode. The effect

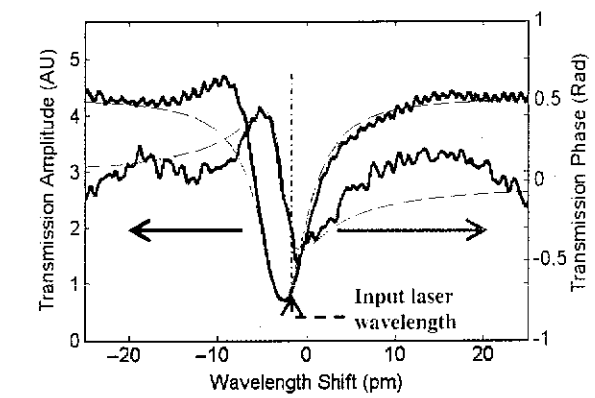

Fig. 15. Solid (dashed) lines show measured (simulated) transmission amplitude (right) and phase (left) of the coupled waveguide and microdisk cavity without AFM tip perturbation.

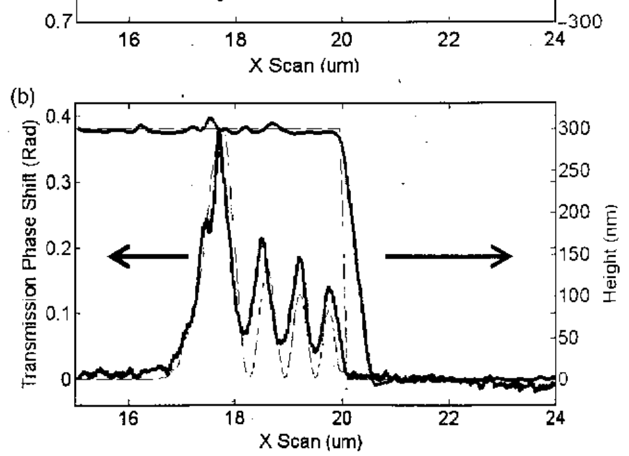

Fig. 16. (a) Solid blue lines show the transmission amplitude (top) and phase (down) of the coupled waveguide and microdisk cavity as AFM tips scan the microdisk cavity in the radial direction. Dashed blue lines (left) show the radial pattern of the normalized electrical field intensity. (b) The solid (dashed) red curves show the actual (ideal) AFM topography scan.

of AFM tip perturbation on the coupled waveguide-cavity device is mainly causing a positive phase shift and a reduction in the transmission amplitude. Considering the fact that the input laser is red shifted with respect to the unperturbed resonant mode of the cavity (refer to Fig. 15), these changes in the transmission amplitude and phase are mainly contributed by a red shift in the resonant mode of the cavity caused by the AFM tip perturbation. If the loss due to scattering and absorption was dominant, it would have resulted in an increase in the transmission amplitude and a reduction in the transmission phase (caused by the reduction in the intrinsic Q of the cavity). Thus, we conclude that the major effect of the AFM tip is to introduce a shift in the resonance wavelength of the microdisk. The amount of the shift in the cavity resonance is proportional to the electrical field intensity at the tip position. The maximum shift appears when the tip is at the position corresponding to the maximum field intensity of the main resonant mode lobe. The amount of the wavelength shift can be calculated from both amplitude and phase responses and in both cases result in very similar shifts of about 1.25 pm.

Thus, we have developed a near-field imaging technique that provides a powerful tool for the direct investigation of the optical modes of microdisk resonators with sub-wavelength (~20 nm) spatial resolution. The use of heterodyne detection enables us to explicitly obtain the complex optical response (i.e., amplitude and phase response) of the microresonator. This then permits us to deconvolve the effect of the scanning AFM tip on cavity loss, scattering and dispersion, and obtain the exact mode profile of the resonator mode.

2.2. Planar SiN Resonators

Ultra-high-quality factor optical microresonators, with their long photon lifetime, high field intensities, and sharp resonant frequency features, have proven to be very good candidates for sensing and detection applications. However, despite their good performance in the infrared portion of the spectrum, silicon resonators suffer from significant material loss in the visible range of the optical spectrum, making them unsuitable for visible light applications such as florescence and surface enhanced Raman spectroscopy (SERS). Realization of visible high-Q optical microresonator structures on silicon based material systems has great benefits, such as ease of fabrication, integrability with mature silicon electronics and low cost. High Q microresonator structures have already been demonstrated on silicon oxide,[56] silicon,[27] and silicon nitride materials.[30] While SiOx microtoroid and microsphere resonators have shown the highest quality factors,[56] their size and lack of chip-scale integrability (because of the bulky fiber taper coupling scheme) results in complications in using them for integrated photonics applications. Silicon nitride (SiNx), on the other hand, offers a very low material loss throughout the optical range (wavelengths from 300 nm to several microns), and moderately high refractive index (~2.0), making it a very good candidate for the mentioned applications. In this section, we show our recent result on the demonstration of monolithic, high quality factor, compact Si_3N_4 resonators on SiO_2 (without undercutting) critically coupled to in-plane waveguides at λ = 655 nm.[57,58]

Fabrication of these structures is done on a thin layer of Si_3N_4 on top a thick 6 μm isolating thermal oxide layer covering the Si substrate. A thin layer of electron beam resist is then spun on the samples and waveguides and microdisks with several different coupling gaps are patterned using electron beam lithography. The low damage etching is optimized using an ICP plasma etcher with CF_4 etch chemistry. The high quality of the etched walls, especially in the gap region between the resonator and the waveguide is evident from Figure 17.

Owing to the large refractive index and low loss of SiN in the visible wavelength range, the ultimate Q in these resonators is limited only by the surface roughness. A typical edge roughness of SiN nanophotonic waveguides is shown in Figure 17. For a microdisk resonator with r = 20 μm, from the dips in the transmission spectrum, we obtain $Q \sim 5 \times 10^5$, while larger (r = 100 μm) microdisks exhibit $Q \sim 4 \times 10^6$. As seen in the transmission spectrum of Figure 18, although different radial modes differ in their respective effective index and phase mismatch to the waveguide, ($n_{WG} = 1.7$, $n_{disk,1} = 1.73$, $n_{disk,2} = 1.68$, $n_{disk,3} = 1.63$) several modes are coupled to the waveguide. (The free spectral range of the first order mode is 1.7 nm and the five larger dips in the transmission were identified to be due to the first radial mode.)

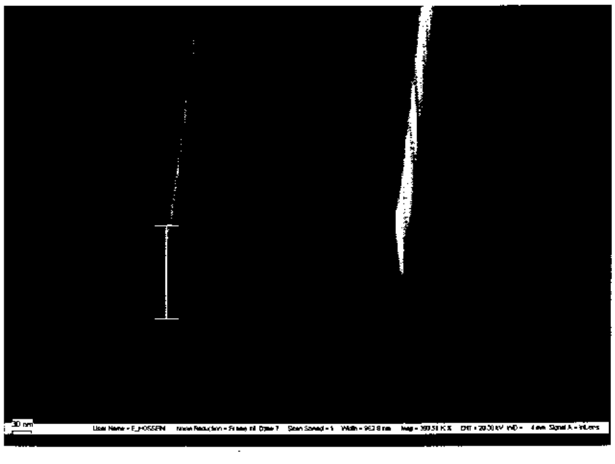

Fig. 17. SEM image of smooth sidewalls for a SiN waveguide is shown. To isolate the nitride layer from the lossy and high index Si substrate, 6 μm of oxide is initially grown on the substrate and SiNx is deposited on the oxide. Reproduced with permission from [57], E. S. Hosseini et al., High quality factor microdisk resonators for chip-scale visible sensing. *IEEE Lasers and Electro-Optics Society, 2008. LEOS 2008. 21st Annual Meeting* November **(2008)**, Vol. 342–343. © 2008, IEEE.

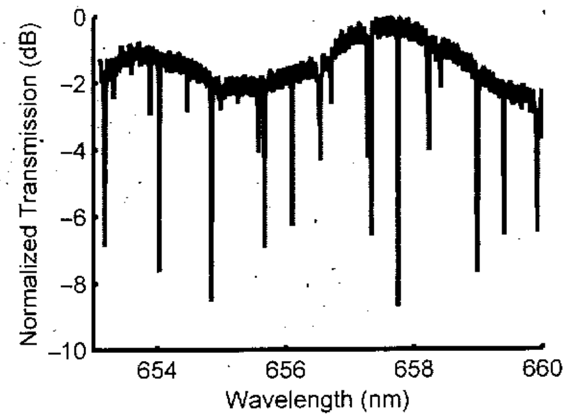

Fig. 18. Transmission spectrum of the waveguide-coupled SiN microdisk resonator with the first order radial modes optimally coupled to the straight waveguide. Reproduced with permission from [57], E. S. Hosseini et al., High quality factor microdisk resonators for chip-scale visible sensing, *IEEE Lasers and Electro-Optics Society, 2008. LEOS 2008. 21st Annual Meeting* November **(2008)**, Vol. 342–343. © 2008, IEEE.

Finally, we conclude by observing that the resonance wavelengths for these SiN microdisk resonators overlap with the available noble metal plasmon resonances. Hence, such resonators, when coupled efficiently with patterned metallic nanostructures on the surface, could potentially enable cascaded SERS enhancement owing to the long cavity photon lifetime, huge field enhancement, and ultimately ultra-sensitive SERS sensors. Moreover, the compact size of the resonator enables dense integration and multiplex sensing, with the potential for CMOS compatibility and Si-based substrates for future integration of optical and optoelectronic functionalities.

3. IMPACT AND PROSPECTS

3.1. Chip-Scale Multiplex Sensing

The high Q and small mode volume of microresonators on CMOS compatible substrates, enables realization of label-free sensors and dense integrated sensor arrays, where sensing is obtained by transcribing the refractive index change due to a surface binding (to a specific coating on the microresonator surface), to a resonance wavelength shift. The small interrogation volume due to the ultra-compact device size makes such microresonator based sensors more sensitive to the total bound mass. Moreover, one of the major advantages of compact integrated platforms for sensing applications is the possibility of including several sensing devices in the same system for monitoring different properties or different target agents in a specimen. Figure 19 shows a possible configuration based on paired resonators in a MZ interferometer in which different planar resonators are selectively covered with coatings that are sensitive to different target particles in the sample. Note that the choice of proper coatings plays an important role in the final selectivity of the sensor in targeting specific agents of interest. The development of such coatings has been subject to extensive research[59,60] during recent years, and well-known conventional coatings can be used for most practical applications. Furthermore, the development of selective area printing techniques[61,62] allows us to put the coating of interest specifically on desired resonators in implementation of these multiplexed sensing devices. Eventually, in the fabricated devices, by monitoring the spectral peaks corresponding to each resonator at the output of the spectrometer, it is possible to obtain information about the presence and concentration of each of the target substances in a parallel fashion. Moreover, the small size of the sensor array, could enable handheld compact sensors for multiplexed detection of an array of target molecules.

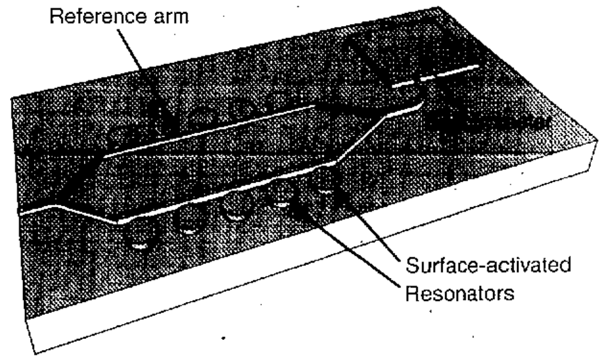

Fig. 19. Schematic of the multiplexed sensor device based on MZI and microdisk resonators.

3.2. Reconfigurable Optical Signal Processing

Using coupled microresonator and waveguide structures as primary building elements, a more ambitious and general framework is being actively pursued by several research groups, wherein, multi-input multi-output (MIMO) optical processing block that can be adjusted to realize any desired transfer function matrix that lies within the limits defined by the system specifications. In this case, the reconfigurable cellular photonic arrays (RCPAs) is based on tunable cross-connected element matrices at the input and output and an array of processing unit cells, with the input/output switch matrices provide optical signal routing between different unit cells and also can provide the functionality of a complex matrix transformation on a vector of optical signals by weighted combination of different input signals. The processing unit cell on the other hand can be cascaded to realize the desired optical filters which combine with the input output transformation to realize the desired MIMO transfer function.

A particular implementation of such a reconfigurable process has been demonstrated for optical CDMA recently,[63] wherein the building block elements composed of such optical circuits containing tunable filters and tunable phase controllers, offer rapidly reconfigurable spectral phase encoders (SPE) and decoders for optical code division multiple access (OCDMA). Potential application of such reconfigurable optical signal processing modules covers a wide range of applications in both military and civil sectors, including but not limited to broadband optical and microwave communication networks and broadband signal processing is the electronic war circumstance.

3.3. On-Chip Optical Amplification and Lasing

While this paper is focused on passive microresonators on CMOS compatible substrates, the incorporation of active functionalities, such as optical gain, lasing and photodetection is critical, in order to satisfy several emerging applications in chip-scale optical interconnects.[64] In this regard, two major approaches are being pursued. The first approach is based on the hybrid combination of the low-loss, low-cost CMOS Si-based photonics devices with the active functionality available from III–V compound semiconductors. Impressive progress has been achieved in realization hybrid amplifiers and lasers using the hybrid AlGaInAs-silicon platform where the InP active and silicon passive components are integrated using wafer bonding.[65] An alternate approach being investigated is to incorporate Erbium into the Silicon or into the cladding SiO_2 layers, to achieve optical gain. Here, some major challenges remain; however, progress is being achieved.[66] The realization of such chip-scale optical amplifiers and lasers in Si-based waveguides would be a major milestone and could be a technology enabler for several applications in chip-scale optical interconnects and for the future on-chip optical routing in multi-processor cores.[64]

4. CONCLUSIONS

In conclusion, we have reviewed recent progress in designing, fabricating and characterizing high-Q traveling-wave microresonators on CMOS compatible substrates, with a focus on ultra-compact Si-based microring and microdisk resonators in the visible and near infrared wavelengths with ultra-high Q and small mode volume, suitable for strong light-matter interaction. Systematic analysis and design of single and coupled-resonator filters was provided. Furthermore, by using a thermal model we demonstrated optimized microresonator structures with improved thermal conductivity that can sustain a high circulating optical intensity at the resonance wavelength, which is particularly useful for nonlinear optics and optical signal processing applications.

The extensive mature manufacturing expertise readily available in the current CMOS foundries and the possibility of realizing hybrid systems with electronic components on the same chip enables realization of complex chip-scale systems with a multitude of functionalities for the communication, sensing, and signal processing areas. Future prospects of such microresonators in CMOS-compatible substrate technology include portable multi-purpose bio/chemical sensing systems, reconfigurable optical signal processing modules and chip-scale optical amplifiers and lasers.

Acknowledgments: This work was supported by the Air Force Office of Scientific Research (G. Pomrenke) and the Air Force Presidential Early Career Award for Scientists and Engineers (PECASE).

References and Notes

1. D. W. Vernooy, A. Furusawa, N. P. Georgiades, V. S. Ilchenko, and H. J. Kimble, *Phys. Rev. A* 57, R2293 (**1998**).
2. S. L. McCall, A. F. J. Levi, R. E. Slusher, S. J. Pearton, and R. A. Logan, *Appl. Phys. Lett.* 60, 289 (**1992**).
3. F. Vollmer, D. Braun, A. Libchaber, M. Khoshsima, I. Teraoka, and S. Arnold, *Appl. Phys. Lett.* 80, 4057 (**2002**).
4. F. Vollmer and S. Arnold, *Nature Methods* 5, 591 (**2008**).
5. R. K. Chang and A. J. Campillo, Optical Processes in Microcavities, World Scientific, Singapore (**1996**).
6. E. A. J. Mercatili, *Bell Syst. Tech. J.* 48, 2103 (**1969**).
7. R. Beausoleil, J. Ahn, N. Binkert, A. Davis, D. Fattal, M. Fiorentino, N. P. Jouppi, M. McLaren, C. M. Santori, R. S. Schreiber, S. M. Spillane, D. Vantrease, and Q. Xu, A Nanophotonic Interconnect for High-Performance Many-Core Computation, Integrated Photonics and Nanophotonics Research and Applications, paper ITuD2 (**2008**).
8. T. Barwicz, H. Byun, F. Gan, C. W. Holzwarth, M. A. Popovic, P. T. Rakich, M. R. Watts, E. P. Ippen, F. X. Kärtner, H. I. Smith, J. S. Orcutt, R. J. Ram, V. Stojanovic, O. O. Olubuyide, J. L. Hoyt, S. Spector, M. Geis, M. Grein, T. Lyszczarz, and J. U. Yoon, *J. Opt. Netw.* 6, 63 (**2007**).
9. G. C. Valley, *Opt. Express* 15, 1955 (**2007**).
10. F. X. Kärtner, R. Amatya, M. Araghchini, J. Birge, H. Byun, J. Chen, M. Dahlem, N. A. DiLello, F. Gan, C. W. Holzwarth, J. L. Hoyt, E. P. Ippen, A. Khilo, J. Kim, M. Kim, A. Motamedi, J. S. Orcutt, M. Park, M. Perrott, M. A. Popovic, R. J. Ram, H. I. Smith, G. R. Zhou, S. J. Spector, T. M. Lyszczarz, M. W. Geis, D. M. Lennon, J. U. Yoon, M. E. Grein, and R. T. Schulein, *Proc. SPIE* 6898, 689806 (**2008**).
11. C. Monat, P. Domachuk, and B. J. Eggleton, *Nat. Photonics* 1, 106 (**2007**).
12. K. De Vos, I. Bartolozzi, E. Schacht, P. Bienstman, and R. Baets, *Opt. Express* 15, 7610 (**2007**).
13. S. Mandal and D. Erickson, *Opt. Express* 16, 1623 (**2008**).
14. K. J. Vahala, *Nature* 424, 839 (**2003**).
15. K. Vahala, Optical Microcavities, World Scientific, Singapore, (**2004**).
16. R. A. Soref and J. P. Lorenzo, *IEEE J. Quantum Electron.* 22, 873879 (**1986**).
17. G. T. Reed and A. P. Knights, Silicon Photonics: An Introduction, John Wiley, West Sussex, (**2004**).
18. L. Pavesi and D. J. Lockwood, Silicon Photonics, Springer-Verlag, New York (**2004**).
19. M. Lipson, *J. Lightwave Technol.* 23, 4222 (**2005**).
20. S. F. Preble, Q. Xu, B. S. Schmidt, and M. Lipson, *Opt. Lett.* 30, 2891 (**2005**).
21. V. R. Almeida, C. A. Barrios, R. R. Panepucci, and M. Lipson, *Nature* 431, 1081 (**2004**).

22. A. Liu, R. Jones, L. Liao, D. Samara-Rubio, D. Rubin, O. Cohen, R. Nicolaescu, and M. Paniccia, *Nature* 427, 615 (**2004**).
23. S. J. Emelett and R. Soref, *J. Lightwave Technol.* 23, 1800 (**2005**).
24. O. Boyraz and B. Jalali, *Opt. Express* 12, 5269 (**2004**).
25. H. Rong, R. Jones, A. Liu, O. Cohen, D. Hak, A. Fang, and M. Paniccia, *Nature* 433, 725 (**2005**).
26. M. Borselli, K. Srinivasan, P. E. Barclay, and O. Painter, *Appl. Phys. Lett.* 85, 3693 (**2004**).
27. M. Borselli, T. J. Johnson, and O. Painter, *Opt. Express* 13, 1515 (**2005**).
28. T. J. Johnson, M. Borselli, and O. Painter, *Opt. Express* 14, 817 (**2006**).
29. J. Niehusmann, A. Vörckel, P. H. Bolivar, T. Wahlbrink, W. Henschel, and H. Kurz, *Opt. Lett.* 29, 2861 (**2004**).
30. P. E. Barclay, K. Srinivasan, O. Painter, B. Lev, H. Mabuchi, *Appl. Phys. Lett.* 89, 131108 (**2006**).
31. A. Yariv, *Electron. Lett.* 36, 321 (**2000**).
32. M. Cai, O. Painter and K. J. Vahala, *Phys. Rev. Lett.* 85, 74 (**2000**).
33. R. J. Hoekstraa, M. J. Kushnerb, V. Sukharev, P. Schoenborn, *J. Vac. Sci. Technol. B* 16, 2102 (**1998**).
34. M. Soltani, S. Yegnanarayanan, Q. Li, and A. Adibi, Systematic Engineering of Waveguide-Resonator Coupling for Silicon Microring/Microdisk/Racetrack Resonators: Theory and Experiment, Under preparation.
35. M. Soltani, S. Yegnanarayanan, and A. Adibi, *Opt. Express* 15, 4694 (**2007**).
36. H. Haus, Waves and Fields in Optoelectronics, Prentice-Hall, Englewood Cliffs, New Jersey (**1984**).
37. F. Xia, L. Sekaric, and Y. A. Vlasov, *Opt. Express* 14, 3872 (**2006**).
38. P. Barclay, K. Srinivasan, and O. Painter, *Opt. Express* 13, 801 (**2005**).
39. T. Carmon, L. Yang, and K. J. Vahala, *Opt. Express* 12, 4742 (**2004**).
40. M. Soltani, Q. Li, S. Yegnanarayanan, and A. Adibi, *Opt. Express* 15, 17305 (**2007**).
41. B. E. Little, S. T. Chu, P. P. Absil, J. V. Hryniewicz, F. G. Johnson, F. Seiferth, D. Gill, V. Van, O. King, and M. Trakalo, *IEEE Photon. Technol. Lett.* 16, 2263 (**2004**).
42. T. Barwicz, M. A. Popovic, M. R. Watts, P. T. Rakich, E. P. Ippen, and H. I. Smith, *J. Lightwave Technol.* 24, 2207 (**2006**).
43. Q. Li, M. Soltani, S. Yegnanarayanan, and A. Adibi, *Opt. Express* 17, 2247 (**2009**).
44. M. A. Popovic, C. Manolatou, and M. R. Watts, *Opt. Express* 14, 1208 (**2006**).
45. Q. Li, S. Yegnanarayanan, A. Atabaki, and A. Adibi, Calculation and Correction of Coupling-Induced Resonance Frequency Shifts in Traveling-Wave Dielectric Resonators, *Integrated Photonics and Nanophotonics Research and Applications Topical Meeting*, Optical Society of America, Washington, DC, USA (**2007**).
46. F. Xia, M. Rooks, L. Sekaric, and Y. Vlasov, *Opt. Express* 15, 11934 (**2007**).
47. D. Xu, A. Densmore, P. Waldron, J. Lapointe, E. Post, A. Delage, S. Janz, P. Cheben, J. H. Schmid, and B. Lamontagne, *Opt. Express* 15, 3149 (**2007**).
48. J. K. S. Poon, J. Scheuer, S. Mookherjea, G. T. Paloczi, Y. Huang, and A. Yariv, *Opt. Express* 12, 90 (**2004**).
49. B. E. Little, S. T. Chu, H. A. Haus, J. Foresi, and J.-P. Laine, *J. Lightwave Technol.* 15, 998 (**1997**).
50. S. Xiao, M. H. Khan, H. Shen, and M. Qi, *Opt. Express* 15, 14765 (**2007**).
51. P. Meystre and M. Sargent, III, Elements of Quantum Optics, Springer-Verlag, Berlin (**1991**).
52. Y. Inouye and S. Kawata, *Opt. Lett.* 19, 159 (**1994**).
53. J. T. Robinson, S. F. Preble, and M. Lipson, *Opt. Express* 14, 10588 (**2006**).
54. A. A. Eftekhar, M. Soltani, S. Yegnanarayanan, and A. Adibi, Sub-wavelength imaging of optical modes on silicon microdisk cavities using a near-field probing technique, *IEEE/LEOS Winter Topicals Meeting Series 2009*, January (**2009**), Vol. 92–93.
55. A. A. Eftekhar, M. Soltani, S. Yegnanarayanan, and A. Adibi, Characterization of the effect of small perturbations on the optical modes in high Q microdisk cavities, *IEEE Lasers and Electro-Optics Society, LEOS 2008, 21st Annual Meeting*, November (**2008**), Vol. 314–315.
56. D. K. Armani, T. J. Kippenberg, S. M. Spillane and K. J. Vahala, *Nature* 421, 925 (**2003**).
57. E. S. Hosseini, S. Yegnanarayanan, and A. Adibi, High quality factor microdisk resonators for chip-scale visible sensing, *IEEE Lasers and Electro-Optics Society, 2008. LEOS 2008. 21st Annual Meeting* November (**2008**), Vol. 342–343.
58. E. S. Hosseini, S. Yegnanarayanan, A. H. Atabaki, M. Soltani, and A. Adibi, *Opt. Express* 17, 14543 (**2009**)
59. M. Thust, M. J. Schöning, P. Schroth, Ü. Malkoc, C. I. Dicker, A. Steffen, P. Kordos and H. Lüth, *J. Molecular Catalysis* B 7, 77 (**1999**).
60. S. S. Iqbal, M. W. Mayo, J. G. Bruno, B. V. Bronk, C. A. Batt, and J. P. Chambers, *Biosensors and Bioelectronics* 15, 549 (**2000**).
61. M. J. Feldstein, J. P. Golden, C. A. Rowe, B. D. MacCraith, and F. S. Ligler, *Biomed. Microdevices* 1, 139 (**1999**).
62. H. B. Lu, J. Homola, C. T. Campbell, G. G. Nenninger, S. S. Yee, and B. D. Ratner, *Sensors Actuators B* 74, 91 (**2001**).
63. A. Agarwal, P. Toliver, R. Menendez, S. Etemad, J. Jackel, J. Young, T. Banwell, B. E. Little, S. T. Chu, C. Wei, C. Wenlu, J. Hryniewicz, F. Johnson, D. Gill, O. King, R. Davidson, K. Donovan, and P. J. Delfyett, *J. Lightwave Technol.* 24, 77 (**2006**).
64. A. Shacham, K. Bergman, L. P. Carloni, *IEEE Trans. Computers* 57, 1246 (**2008**).
65. A. W. Fang, R. Jones, H. Park, O. Cohen, O. Raday, M. J. Paniccia, and J. E. Bowers, *Opt. Express* 15, 2315 (**2007**).
66. C. P. Michael, H. B. Yuen, V. A. Sabnis, T. J. Johnson, R. Sewell, R. Smith, A. Jamora, A. Clark, S. Semans, P. B. Atanackovic, and O. Painter, *Opt. Express* 16, 19649 (**2008**).

Received: 24 February 2009. Accepted: 31 March 2009.